

# Australia Telescope Search for Cosmic Microwave Background Anisotropy

Ravi Subrahmanyan<sup>1,2</sup>, Michael J. Kesteven<sup>2</sup>, Ronald D. Ekers<sup>2</sup>,  
Malcolm Sinclair<sup>2</sup>, Joseph Silk<sup>3</sup>

<sup>1</sup> *Raman Research Institute, Sadashivanagar, Bangalore 560 080, India*

<sup>2</sup> *Australia Telescope National Facility, CSIRO, PO Box 76, Epping, NSW 2121, Australia*

<sup>3</sup> *Departments of Astronomy and Physics and Centre for Particle Astrophysics, University of California, Berkeley, CA 94720, USA*

## ABSTRACT

In an attempt to detect cosmic microwave background (CMB) anisotropy on arcmin scales, we have made an 8.7-GHz image of a sky region with a resolution of two arcmin and high surface brightness sensitivity using the Australia Telescope Compact Array (ATCA) in an ultra-compact configuration. The foreground discrete-source confusion was estimated from observations with higher resolution at the same frequency and in a scaled array at a lower frequency. Following the subtraction of the foreground confusion, the field shows no features in excess of the instrument noise. This limits the CMB anisotropy flat-band power to  $Q_{flat} < 23.6 \mu\text{K}$  with 95 per cent confidence; the ATCA filter function\*  $F_l$  in multipole  $l$ -space peaks at  $l_{eff} = 4700$  and has half maximum values at  $l = 3350$  and  $6050$ .

**Key words:** cosmic microwave background – cosmology: observations – techniques: interferometric.

## 1 INTRODUCTION

Anisotropies in the cosmic microwave background (CMB)

are usually described in terms of the coefficients  $C_{lm}$  of their spherical harmonic decomposition;  $C_l = \langle |C_{lm}|^2 \rangle$  represents the anisotropy power at multipole order  $l$ . Sachs-Wolfe anisotropies in a scale-invariant matter power spectrum give flat  $l(l+1)C_l$  and any experiment sensitive to CMB anisotropies in an  $l$ -space window  $F_l$  may be expected to measure a sky temperature variance

$$(\Delta T)^2 = \sum_l \frac{6(2l+1)}{5l(l+1)} (Q_{flat})^2 F_l, \quad (1)$$

where  $Q_{flat}$  denotes the quadrupole normalization of a flat CMB anisotropy spectrum. The observing scheme and data analysis procedures determine the window function  $F_l$  for any experiment. The implications of any observed CMB temperature variance  $(\Delta T)^2$  may be quoted in fairly model independent terms by the inferred  $Q_{flat}$ . This  $Q_{flat}$  may be viewed as being a measure of the CMB anisotropy power spectral density within the  $l$ -space window defined by  $F_l$ .

Recent observations of the anisotropy in the CMB on large and intermediate angular scales ( $l \lesssim 500$ ) have begun to provide interesting constraints on theories of structure formation and the parameters of cosmological models (see, for example, Lineveaver and Barbosa (1997) for an updated

compilation of data points and a discussion of their implications).

Primary CMB anisotropies at small angular scales ( $l \gtrsim 500$ ) are expected to be relatively damped in most structure formation models owing to the thickness of the last scattering surface and the diffusion damping of sub-horizon scale baryon fluctuations in the pre-recombination epoch. However, flat-band powers comparable to the  $Q_{flat}$  detected by *COBE DMR* (Bennett et al. 1996) may be predicted at multipoles  $l \gtrsim 500$  in certain cosmological-constant ( $\Lambda$ ) and open-universe manifestations of baryon isocurvature models (Hu & Sugiyama 1994; Hu, Bunn & Sugiyama 1995). The anisotropy power at large  $l$  may be critically dependent on the reionization history: small-scale anisotropies may be suppressed by early reionization.

Secondary anisotropies may be generated at the later last-scattering-surface in a reionized universe predominantly owing to second-order mode coupling between density perturbations and bulk velocities (the ‘Vishniac effect’); this could significantly contribute to arcmin-scale ( $l \gtrsim 10^3$ ) anisotropies particularly if the ionization fraction is high at late times (Hu, Scott & Silk 1994). Persi et al. (1995) estimate that this second-order Doppler effect may contribute a band power  $Q_{flat} \approx 0.2 \mu\text{K}$  at  $l \approx 10^3$  in CDM and CDM+ $\Lambda$  universes and that the anisotropy power may be an order of magnitude higher in certain baryon isocurvature models.

Jones et al. (1997) report the detection of a  $\sim 100 \mu\text{K}$  negative feature in a 2-arcmin resolution image of a sky patch that has no obvious cluster of galaxies along the line of sight in either optical or *ROSAT* X-ray images. A sensitive low-resolution image of a ‘blank’ field with the VLA

\*The ATCA filter function is available at the website

[www.atnf.csiro.au/research/cmb/cmb\\_atca.html](http://www.atnf.csiro.au/research/cmb/cmb_atca.html)

(Richards et al. 1997) is also reported to show a negative feature approximately  $25'' \times 65''$  in size and with a peak central decrement of  $-250 \mu\text{K}$ . It has been suggested that these may be CMB decrements owing to the inverse-Compton scattering of CMB photons, the Sunyaev-Zeldovich (S-Z) effect, in distant concentrations of hot gas. It may be noted that Hattori et al. (1997) recently reported the discovery, in its X-ray emission, of a hot gas concentration at a redshift  $z \approx 1$  whose properties are similar to the gaseous halos in rich clusters of galaxies; however, the ‘cluster’ appears to have only one visible galaxy.

Anisotropies arising from the S-Z effect, in a cosmological population of groups and clusters of galaxies containing hot intra-cluster gas may be an important cause of anisotropy power at  $l \gtrsim 10^3$  (Persi et al. 1995; Bond & Myers 1996). The S-Z anisotropies are generically non-Gaussian and are expected to have phase-correlations between different  $l$  modes; their statistical description requires higher-order correlations apart from the  $C_l$  power spectra. Hot gas in groups and clusters in scale-invariant CDM universes normalized to give  $\sigma_8 = 1$  (the magnitude of dynamical clustering at the present time is quantified by  $\sigma_8$  which is the rms mass fluctuations in  $8h^{-1}\text{-Mpc}$  spheres) is expected to contribute band powers  $Q_{flat} \approx 2 \mu\text{K}$  at  $l \approx 1-5 \times 10^3$  (Bond & Myers 1996). In *COBE*-normalized tilted CDM, MDM and models in which the shape factor  $\Gamma = \Omega_c h$  is approximately 0.2, the predicted  $\sigma_8$  agrees better with galaxy clustering and in these models the band powers at large  $l$  are 1–2 orders of magnitude smaller. The dominant contribution at high  $l$  may come from quasar-ionized hot gas bubbles (Aghanim et al. 1996), whose existence is based on plausible theoretical inferences.

Computations of the expected secondary anisotropies involve non-linear gravitational dynamics and hydrodynamic simulations and are critically dependent on the thermal history of the gas that may in turn depend on the astrophysical evolution in populations that cause the ionization. It follows that observations of the arcmin-scale anisotropy, corresponding to measurements of the CMB anisotropy at  $l \gtrsim 10^3$ , could constrain the structure formation theories.

## 2 OBSERVATIONS WITH THE AUSTRALIA TELESCOPE

The advantages of Fourier-Synthesis imaging telescopes, and in particular the design features of the Australia Telescope Compact Array (ATCA; see The Australia Telescope 1992) that make it specifically advantageous for high-brightness-sensitivity imaging, were detailed in Subrahmanyan et al. (1993) and we restrict ourselves to giving a synopsis of the methodology here. Our observing strategy has been to make full Earth-rotation synthesis observations of ‘empty’ fields in a special ultra-compact 122-m array configuration – with five 22-m diameter antennae located 30.6 m apart in an E-W line – in order to maximize the brightness sensitivity of the imaging. The three baselines between antennae spaced 61 m apart are used to construct a model of the foreground confusion; this is then subtracted from all of the visibility data and the four baselines between antennae 30.6 m apart are used to synthesize an image with high brightness sensitivity. Because the confusing sources are measured simultaneously and using baselines between the very same antennae,

errors in the estimation of confusion owing to variability in the foreground sources and calibration errors are eliminated. Deconvolution errors are avoided because the confusion is estimated as a model fit to visibility data. These observations were made at the highest available frequency of 8.7 GHz to minimize discrete source confusion.

The field was separately observed in a nearly scaled 244-m array at 4.7 GHz, with five ATCA antennae spaced 61-m apart along the E-W line, to examine the spectral indices of any features identified in the region as foreground sources and ensure that the sources subtracted indeed have spectra consistent with optically-thin thermal or synchrotron emission. If the 4.7-GHz images are made with the same sensitivity to point-source flux density as the 8.7-GHz images, the lower-frequency images that are made with the same angular resolution would be less sensitive to CMB temperature fluctuations by a factor  $(4.7/8.7)^\alpha$ , where  $\alpha = 2$  is the spectral index of the CMB anisotropy at these frequencies. However, the 4.7-GHz images would have a relatively greater sensitivity to extended synchrotron emission by a factor  $(4.7/8.7)^\alpha$ , where  $\alpha \lesssim -0.7$  is now the steep spectral index of extended synchrotron sources. To summarize, the 4.7-GHz image could potentially reveal extended foreground sources that may be resolved, and therefore absent, in the 61-m baseline data obtained at 8.7 GHz.

Sky regions – selected using radio source catalogues to be relatively devoid of bright sources – were first imaged at 20-cm wavelength with the ATCA. An examination of these images led to the selection of a field centre which had no sources with flux densities exceeding 1 mJy (at 20-cm wavelength) within 7 arcmin radius (the ATCA antennae have the first null of the 8.7-GHz primary beam at 7 arcmin). The J2000.0-epoch coordinates of the field centre are RA:  $03^h 16^m 26^s.00$ , DEC:  $-49^\circ 47' 57''.00$ . The field has been chosen to be located close to declination  $-50^\circ$  so that the projected antenna spacing is as close as possible without shadowing to the 22-m antenna diameter at large hour angles: this maximizes the brightness sensitivity of the array.

The field was originally observed in 1991 July–August and December in the 122-m array and using a pair of 128-MHz bands centred at 8640 and 8768 MHz; results of the observations made during these periods were reported in Subrahmanyan et al. (1993). Subsequently, the 8.7-GHz front-end amplifiers were changed to HEMT devices and the system temperature at this frequency improved from about 75 to 43 K. The field was reobserved in 1994 July in the 122-m array using the same pair of bands. The total effective observing time obtained in this array now corresponds to about 50 h integration with a system temperature of 43 K and two 128-MHz bands. The rms sensitivity of the imaging has improved by a factor 1.6 as a result of the additional observations made with the improved receivers. All observations were made in dual polarizations. The array phase centres during the observations were offset about  $1^\circ$  from the antenna pointing centres so that imaging artefacts that often appear at the phase centre may be well removed from the sky region of interest. Off-line, the visibility data were phase-corrected to align the array phase centres with the field centre positions, calibrated in amplitude, phase and for the band-pass response, averaged in frequency over a useful band of 112 MHz. The flux-density scale was set by adopting values of 2.84 and 2.79 Jy respectively for the primary

calibrator source PKS 1934–638 at the frequencies 8640 and 8768 MHz (Reynolds 1994).

In 1995 March, the field was observed in a 244-m array at 4800 MHz. The observing and calibration procedure adopted was the same as for the 122-m array observations; the flux-density scale was set by adopting a value of 6.22 Jy for the primary calibrator PKS 1934–638 at this frequency.

All images shown below were made using visibilities with ‘natural’ weighting so as to obtain a high signal-to-noise ratio, the gridding, Fourier transformations and deconvolution, if attempted, were done using the AIPS routine IMAGR. All displayed images are centred at the coordinates of the field centre and, unless explicitly stated, have not been deconvolved. All images shown are in Stokes I and have not been corrected for the attenuation owing to the primary beam. The locus of the first null in the primary beam pattern at 8704 MHz, located at a radius of 7 arcmin, is shown in all the images as a dot-dashed circle.

### 3 ANALYSIS OF THE OBSERVED FIELD

An image of the field made at 4.8 GHz using the 61 and 122-m baselines of the 244-m array observations is shown in Fig. 1. The image has been deconvolved and has a resolution of 1.4 arcmin. Within a radius of 3 arcmin, corresponding to the half-power radius of the ATCA primary beam at 8.7 GHz, three prominent sources are apparent and all these are detected with peak flux density exceeding 10 times the image thermal noise.

In Fig. 2 we show an image of this field at 8.7 GHz that has been constructed using just the four 30.6-m baselines. This image has not been deconvolved, but clearly shows three peaks at the positions of the three sources apparent in the 4.8-GHz image. It may be noted that the synthesized beam sidelobes are very large for this image because of the poor  $u, v$  coverage (only a single spacing – 30.6 m – has been used in the imaging).

The low-resolution 8.7-GHz image of the field (Fig. 2) has a high surface brightness sensitivity, but is confusion limited owing to discrete sources in the field. We estimate the foreground confusion owing to discrete sources in this field using the data obtained in the longer ( $> 30.6$  m) baselines. However, we have restricted ourselves to using just the 61-m baseline (omitting the 92 and 122 m baselines) for deriving the confusion model so that the synthesized beam is only a factor of two smaller as compared to that for the high-surface-brightness image (Fig. 2) from which the confusion is to be subtracted. This may ensure that confusion structures on scales up to about an arcmin, if present, may be included in the confusion model.

We next show a deconvolved image of the field made at 8.7 GHz using the 61-m baselines (Fig. 3). Three sources appear once again, we estimate their positions and flux densities at 8.7 GHz from this deconvolved image and use these parameters as an input model while fitting a 3-component model to the 61-m visibility data. The fit estimated the flux densities of the components to be 274, 182 and 110  $\mu$ Jy. The primary beam at 8.7 GHz is expected to have attenuated the source intensities by factors 0.57, 0.39 and 0.51 respectively. Correcting for this attenuation, the components ought to have flux densities 481, 467 and 216  $\mu$ Jy respectively. We have fit the 4.8-GHz visibilities measured using the 122-m

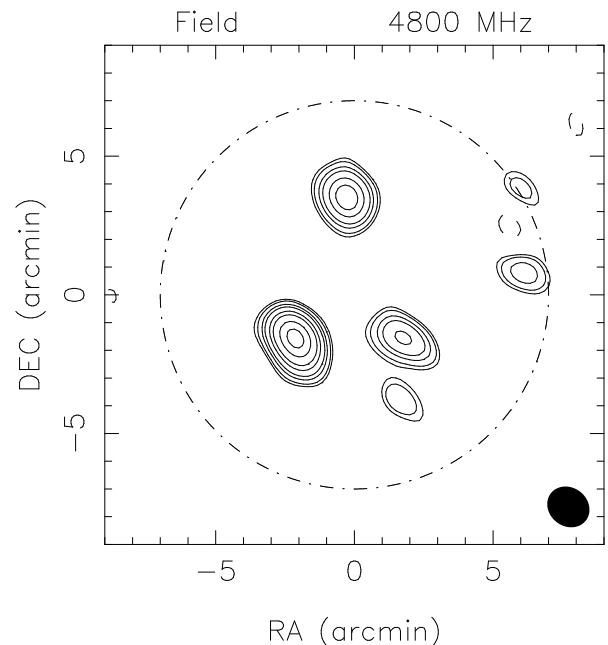


**Figure 1.** Deconvolved image of the field at 4800 MHz made with a beam of  $96 \times 72$  arcsec<sup>2</sup> at a position angle (p.a.) of  $52^\circ$ . Contours at  $27 \mu\text{Jy beam}^{-1} \times (-3, 3, 4, 6, 8, 12, 16, 24, 32)$ . The half-maximum size of the synthesized beam is shown in the bottom right corner as a filled ellipse. In this figure, as also the following three figures, the locus of the first null in the primary beam pattern at 8704 MHz is shown as a dot-dashed circle.

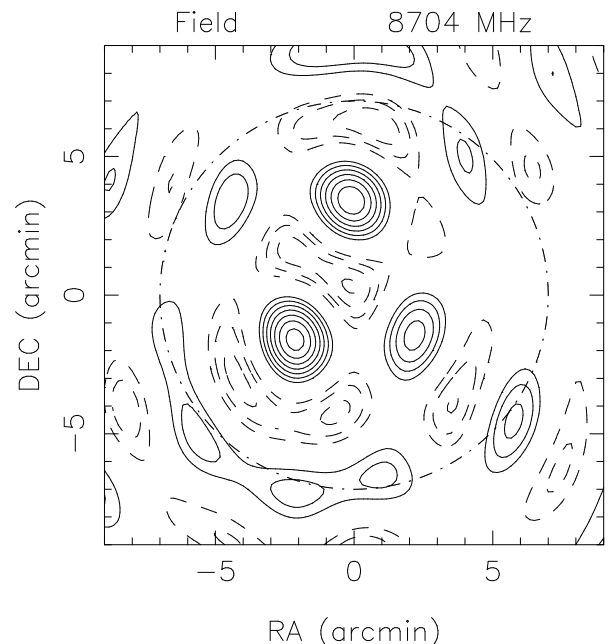


**Figure 2.** An image of the field at 8704 MHz made using just the 30.6-m baselines. The resolution is about 2.2 arcmin. Contours at  $22 \mu\text{Jy beam}^{-1} \times (-10, -8, -6, -4, 4, 6, 8, 10, 12, 14, 16)$ .

baselines (equivalent in angular resolution to the 61 m baselines at 8.7 GHz) to a 3-component model that has component positions fixed at the locations of the sources in the 8.7-GHz, 61-m visibilities: the flux densities of these components are estimated to be 790, 335 and 262  $\mu$ Jy respectively.

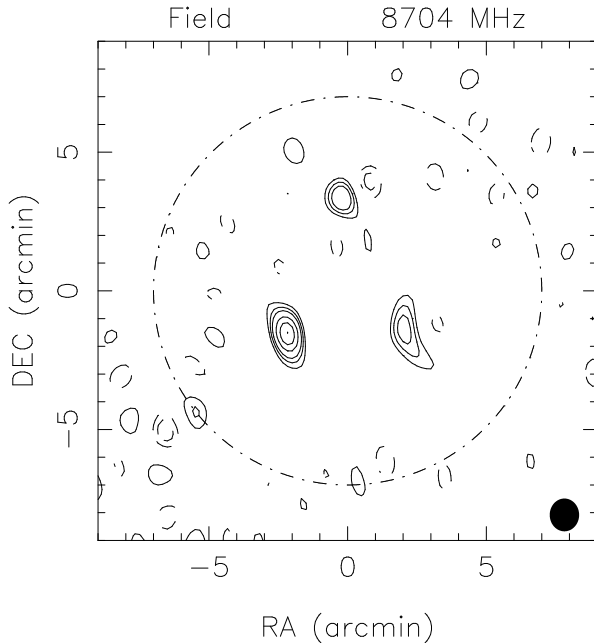


**Figure 3.** A deconvolved image of the field at 8704 MHz made using just the 61-m baselines. The image has a beam FWHM of  $71 \times 57 \text{ arcsec}^2$  at a position angle (p.a.) of  $0^\circ$ . Contours at  $25 \mu\text{Jy beam}^{-1} \times (-4, -3, -2, 2, 3, 4, 6, 8, 10)$ . The half-maximum size of the synthesized beam is shown in the bottom right corner as a filled ellipse.

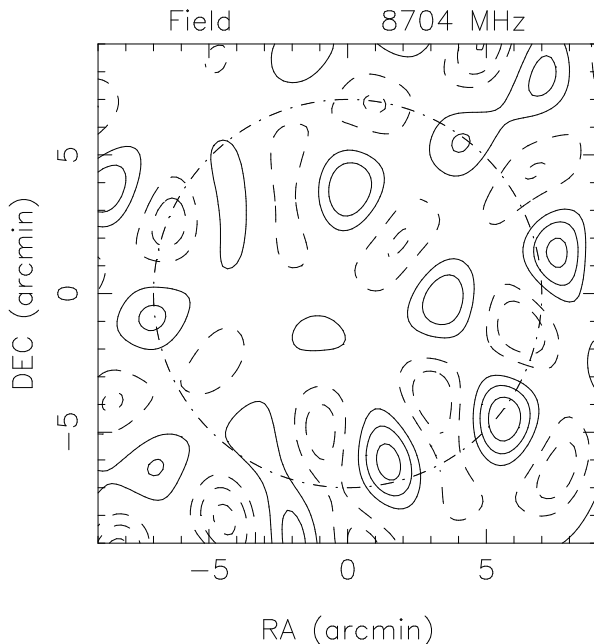


**Figure 4.** The residual image of the field at 8704 MHz following the subtraction of the confusion model; this image has been made using just the 30.6-m baselines. The resolution is about 2.2 arcmin. Contours at  $22 \mu\text{Jy beam}^{-1} \times (-3, -2, -1, 1, 2, 3)$ .

Correcting for the attenuation owing to the primary beam at 4.8 GHz, we estimate the true flux densities of these components to be 934, 439 and  $319 \mu\text{Jy}$  respectively. The derived spectral indices of the components are  $-1.1$ ,  $0.1$  and  $-0.7$  (we define the spectral index  $\alpha$  as  $S_\nu \sim \nu^\alpha$ ); the components

do not have spectral indices  $\alpha = 2$  that would be expected of CMB anisotropies at these frequencies.

The three-component model for the foreground confusion, derived from the fit to the 60-m visibilities obtained at 8.7 GHz, was subtracted from all of the 8.7-GHz visibility data. Following subtraction of the confusion, we constructed an image of the field at 8.7 GHz using just the 30.6-m baselines (Fig. 4). No residual features are apparent in this image. We weighted the image pixel intensities by the primary beam pattern and determined the weighted rms in the primary beam region of the field to be  $21.2 \mu\text{Jy beam}^{-1}$ . The image pixel variance appears consistent with that expected from the telescope thermal noise (see section 4.1), and in sections 5 and 6 below we use this residual image to derive limits on random-phase CMB anisotropy on the 2-arcmin scale corresponding to the resolution in this image.

#### 4 CONTRIBUTORS TO THE IMAGE VARIANCE

The processes which lead to the synthesized image are shown schematically in Fig. 5. The telescope thermal noise, foreground discrete sources and possibly CMB anisotropy contribute to the variance in the synthesized image. CMB anisotropy and foreground radio sources on the sky are attenuated by the primary-beam pattern of the antennae and convolved by the synthesized beam; their contribution may equivalently be viewed as a visibility-domain spatial-frequency filtering of the sky signals as viewed through the primary beam. The telescope thermal noise may be considered to be additive Gaussian random fluctuations, that are characterized by an appropriate angular coherence function, but whose distribution on the sky image has no dependence on the primary beam.

The primary beam plays an important role in the signal path from sky sources to visibility data (or equivalently the synthesized image) and the  $l$ -space filter function that determines the coupling of CMB power to image variance depends on the antenna aperture illumination function. Therefore, instead of modelling the primary beam in the sky plane, we have approximated the aperture illumination by a function whose parameters characterize the central blockage and edge taper (James 1987) and have used parameter values that give an antenna power pattern that fits the measured pattern out to the second null.

The number of independent pixels in the sky image made with just the 30.6-m baseline data, or equivalently the number of degrees of freedom in the variance estimate, may be approximately the number of independent visibility measurements along the 170 m long visibility track. The first null of the ATCA primary beam power pattern is at 7 arcmin radius at 8.7 GHz, this implies that the aperture illumination has an autocorrelation function with an effective diameter of about 17 m and hence the number of independent visibility measurements is about 10.

##### 4.1 Telescope system noise

The image variance resulting from the telescope thermal noise has been measured by two methods. First, by computing the rms over large sky regions well outside the primary beam area where the only contribution to the image

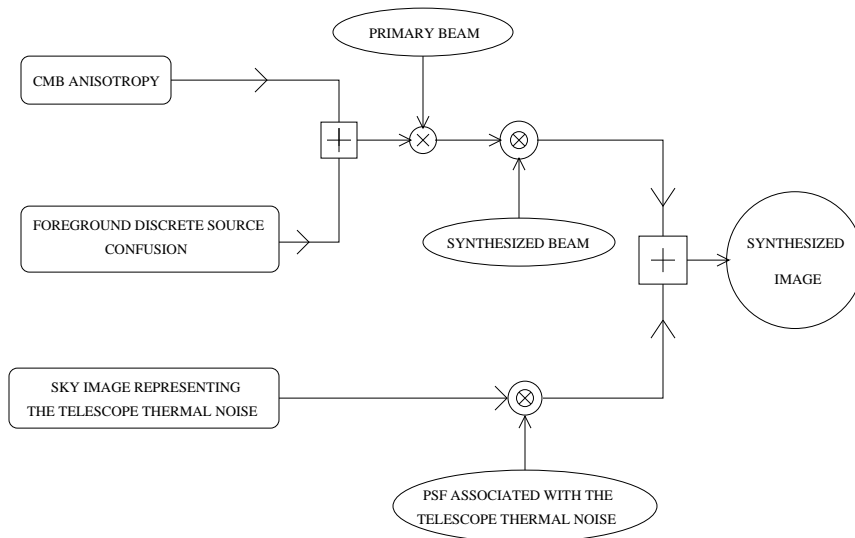


**Figure 5.** The signal flow path. It may be noted that the point spread function (PSF) corresponding to the sky sources – the synthesized beam – may differ from the PSF associated with the telescope thermal noise.

variance is expected to be the telescope thermal noise. Second, by separately imaging the visibilities obtained as the XX and YY correlations between the two orthogonal linear antenna signals X and Y and computing the rms over the  $(XX - YY)/2$  image: the Stokes I component of sources in the field cancel in this combined image and if we assume that the Stokes Q, U and V flux densities are negligible compared to the thermal noise, the system thermal noise will be the only significant contributor to the variance in this combined image. The two methods have yielded consistent values and the rms thermal noise in the sky image is estimated to be  $22.8 \mu\text{Jy beam}^{-1}$  in the image of the field made using the 30.6-m baseline data. Adopting an antenna efficiency of 0.64 at 8.7 GHz (James 1985) the rms noise in the image is consistent with the system temperatures being effectively 72 and 43.5 K respectively during the 1991 and 1994 epoch observations; the later value is in agreement with 1994 epoch measurements of the system temperature made with microwave absorbers placed over the feed horns (Gough 1994).

Along the visibility tracks in the  $u, v$ -domain, the signal-to-noise ratio of the visibility data may vary because, for example, the total system temperature may systematically vary with antenna elevation and hence with position angle in the  $u, v$ -plane, or because data points may have different averaging times. Visibility data are almost never weighted proportional to the rms thermal noise; they are often weighted inversely with the thermal noise variance. Therefore, the image thermal noise is described by a coherence function that is usually not derivable from the synthesized beam. To compute the angular coherence function of the thermal noise, or equivalently the distribution of thermal noise power in the  $u, v$ -domain, we use images made well outside the primary beam area: we compute the 2D autocorrelation function of

these sky images and perform a 2D Fourier transform to the  $u, v$ -domain. This provides us with a  $u, v$ -domain filter appropriate for the telescope thermal noise. Our simulations of the thermal noise component in the sky images have assumed the noise to be Gaussian random, with a power spectrum identical to this 2D  $u, v$ -plane filter function and normalized to give an image rms noise same as the above-mentioned measured values.

The variance in the sky images have been determined by weighting the pixel intensities with the primary beam attenuation. We have simulated images with solely the expected thermal noise contribution, computed the weighted image variances and obtained their distribution function. It may be noted that because the variance estimate is the weighted sum of squares of random variables, the variance is not expected to follow a  $\chi^2$  distribution.

## 4.2 Foreground radio source confusion

The radio sources in the sky are assumed to be Poisson distributed and the differential source count  $N(S)$  is expected to be

$$N(S) = 20.9S^{-2.18} \text{ arcmin}^{-2} \mu\text{Jy}^{-1} \quad (2)$$

at 8.7 GHz, where  $S$  is the source flux density in  $\mu\text{Jy}$  (Partridge et al. 1997 and references therein). The ATCA Fourier-synthesis images have been constructed without any zero-spacing visibility components and at every image pixel position the expectation for the flux density is zero despite the presence of discrete sources in the sky. The expectation of the variance contribution from these sources at any image

position  $(\theta_o, \phi_o)$  is given by

$$\sigma^2 = \int_{\theta, \phi} |b(\theta, \phi)|^2 d\theta d\phi \int_{y=y_{min}}^{y=y_{max}} y^2 N(y) dy, \quad (3)$$

where  $y_{min}$  and  $y_{max}$  are the lower and upper limits to the flux densities of sources present in the sky region and  $b(\theta, \phi)$  represents a beam pattern that is the product of the primary beam centred at the antenna pointing centre and the synthesized beam centred at  $(\theta_o, \phi_o)$ .

We reckon, based on our 1.4-GHz survey of the region, that the field has no sources exceeding about 0.5 mJy at 8.7 GHz. The variance in the image made using the 30.6-m baseline data (Fig. 2) is a factor of two higher than that expected owing to these sources assuming the Partridge et al. source counts. However, there is a reasonable (11 per cent) statistical probability that the ‘excess’ variance in the field is foreground confusion. The number of sources (3) detected with flux density exceeding  $100 \mu\text{Jy}$  – that constitute the model for confusion in the field – and their combined flux density, are also a factor of two larger than expected. A possible explanation for these is that our 3-component model for confusion includes weaker sources that blend and give responses above the detection limit.

Following the subtraction of the confusion model, the residual image shown in Fig. 4 does not show evidence for any significant ‘excess’ variance that may be owing to residual weak foreground sources that have not been included in the model. For the assumed source counts, the expected variance contribution from sources weaker than  $100 \mu\text{Jy}$  is  $(50 \mu\text{Jy beam}^{-1})^2$ . The residual image shown in Fig. 4 has a variance of  $(21.2 \mu\text{Jy beam}^{-1})^2$  and the probability of observing a sample image with a variance as low as this is  $2 \times 10^{-4}$  if sources below  $100 \mu\text{Jy}$  have remained unsubtracted! If we conjecture that the model derived from the 61-m baseline visibility data has incorporated all sources above  $25 \mu\text{Jy}$ , corresponding to the rms thermal noise in the image made with these data, we may then expect that the residual sources in the field that are weaker than this limit may contribute a variance of about  $(33 \mu\text{Jy beam}^{-1})^2$  in images made from the residual 30.6-m baseline data. Even in this optimistic scenario, the probability of observing a sample with a residual variance as low as that in the observed field is as small as 0.3 per cent!

To summarize, the image variance appears to be in excess of the expectation prior to any subtraction of sources, but after the confusion model is subtracted the image variance is below expectations that are derived assuming a minimal residual and unsubtracted confusion. We are led to believe that either the derived confusion model includes sources weaker than  $25 \mu\text{Jy}$ , or perhaps that the faint sources are clustered. We are expanding our observations to several sky regions and expect to have a better understanding of the contribution from confusion following an examination of the residual fluctuations in a larger sky area. While deriving limits on CMB anisotropy in sections 5 and 6 based on our observations of the field, we assume that the residual image has contributions from the telescope thermal noise and CMB anisotropy alone.

We have examined the possibility of using the skew coefficient  $a_3$  as a possible indicator of residual foreground

confusion.  $a_3$  is defined as

$$a_3 = \frac{m_3}{(\sqrt{m_2})^3}, \quad \text{with } m_3 = \sum x_j^3, \quad m_2 = \sum x_j^2 \quad (4)$$

and where the summations are over pixel intensities that are weighted by the primary-beam attenuations at the pixel locations. We find that the image in Fig. 2 has  $a_3 = 0.13$  and the residual image in Fig. 4 has  $a_3 = -0.03$ . Our simulations of foreground confusion show that the derived skew coefficient may be expected to have a standard deviation of as much as 0.57 about the mean skew, and that the expectation for the skew coefficient is just 0.11 and 0.05 respectively if foreground sources below 100 and  $25 \mu\text{Jy}$  remain unsubtracted. Because of the limited number of independent sky pixels in the image of the field, the skew coefficient is not a useful statistic for characterizing the residual confusion; it may prove useful in statistical analyses of future observations that cover multiple fields.

### 4.3 CMB anisotropy

We model the CMB anisotropy as a Gaussian random fluctuation in the sky temperature that is completely described by its power spectrum coefficients  $C_l$ . The expectation for the image variance will then depend on the telescope filter function (TFF)  $F_l$  and the nature of the anisotropy power spectrum over the range in  $l$ -space that corresponds to the pass-band of the filter.

We assume that the anisotropy power spectrum is ‘flat’ in  $l(l+1)$ -space and that the  $C_l$  coefficients are given by

$$C_l = (Q_{flat})^2 \left( \frac{24\pi}{5} \frac{1}{l(l+1)} \right), \quad (5)$$

where  $Q_{flat}$  denotes the quadrupole normalization of the power spectrum. The temperature variance in the sky image is then expected to be

$$(\Delta T)^2 = \sum_l \frac{(2l+1)C_l}{4\pi} F_l \quad (6)$$

and this leads to the expression in equation (1).

We compute the image variance as a weighted mean of the squares of the pixel intensities (image pixel intensities are in units of  $\text{Jy beam}^{-1}$ ) using weights for the intensities that are the primary-beam attenuations at the pixel positions. As discussed in Appendix A, we have computed the ATCA TFFs at the different image pixel locations using equation (A4) and averaged them, using weights that are again the primary-beam attenuations, to obtain the filter function  $F_l$ , in units of  $(\text{Jy beam}^{-1} \text{K}^{-1})^2$ , appropriate to the computed image variance. We have computed the  $F_l$ ’s using the ATCA synthesized beams corresponding separately to the images made with the 30.6 and 61-m baseline data, they are shown in Fig. 6. In the large- $l$  regime of the ATCA  $F_l$ , the expected image variance (in units of  $(\text{Jy beam}^{-1})^2$ ) is approximately given by

$$\Delta S^2 = (Q_{flat})^2 \sum_l \frac{12}{5l} F_l. \quad (7)$$

The TFF corresponding to the 30.6-m baseline data, shown as the continuous line in Fig. 6, is the filter function corresponding to the residual image shown in Fig. 4. It has

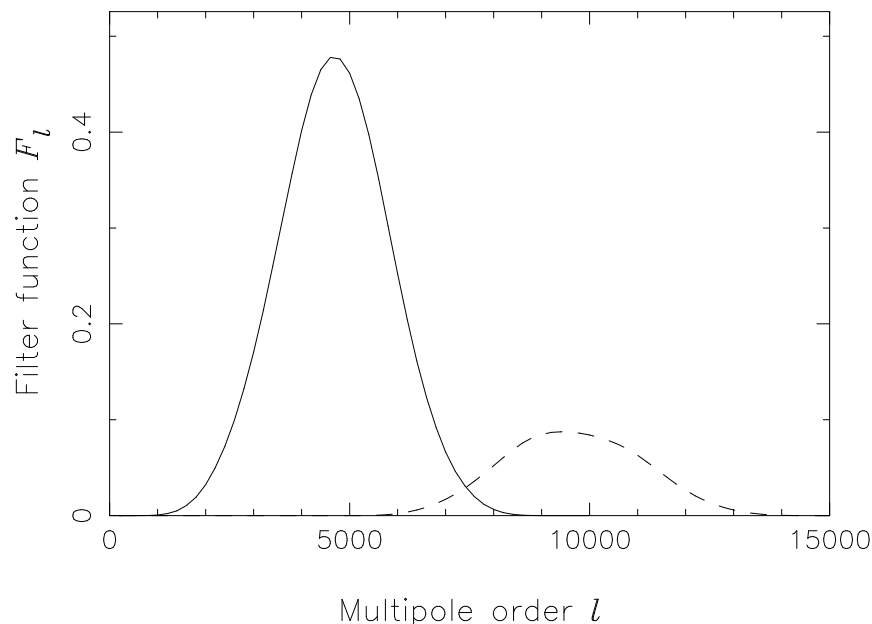


**Figure 6.** ATCA telescope filter function. The continuous line shows the TFF corresponding to the image made with the 30.6-m baseline data, the dashed line shows the filter corresponding to the 61-m baseline data.

a peak of 0.48 at  $l = 4700$  and has half-maximum values at  $l = 3350$  and  $6050$ . Summation over  $l$ -space yields

$$\sum_l \frac{12}{5l} F_l = 0.765 \left( \frac{\mu\text{Jy beam}^{-1}}{\mu\text{K}} \right)^2. \quad (8)$$

If we adopt a ‘flat’ CMB anisotropy spectrum with normalization  $Q_{flat} = 18 \mu\text{K}$  corresponding to the detected power at multipoles  $l \lesssim 20$  (4-yr *COBE DMR* results in Bennett et al. 1996), the expected variance contribution in the 30.6-m baseline image is expected to be  $18^2 \times 0.765 = (15.7 \mu\text{Jy beam}^{-1})^2$ .

A Fourier synthesis telescope with finite-aperture elements measures visibilities that may be considered to be the convolution of the all-sky visibility with the autocorrelation of the antenna aperture illumination. The visibility measurements may be viewed as samples along 1D  $(u, v)$ -tracks of this 2D  $(u, v)$ -plane visibility function. Because the ATCA antenna aperture extends 11 m in radius, its autocorrelation function will extend to a radius of 22 m. It may be noted that this autocorrelation function has a diameter of 44 m which exceeds the spacing between the 1D  $(u, v)$ -tracks corresponding to the 30.6 and 61 m baselines. Therefore, the visibility data along the 30.6 and 61-m baseline visibility tracks are individually averages over regions of the all-sky visibility function and these regions mutually overlap. This results in a partial overlap between the TFFs corresponding to the 30.6 and 61-m visibility data. At any instant, there are three 61-m baselines as compared to four 30.6-m baselines; therefore, the 61-m baseline image is less sensitive to unresolved foreground sources as compared to the 30.6-m baseline data, but by only a factor 0.87. The peak of the TFF corresponding to the 61-m baseline data is 0.087, a fac-

tor 0.18 of the peak of the 30.6-m baseline TFF. Summing over the 61-m baseline TFF,  $\sum 12F_l/(5l) = 0.085$ : CMB anisotropy with a flat spectrum will be expected to contribute a variance in the 61-m baseline image that is a factor 0.11 of the variance in the 30.6-m baseline image. Adopting a normalization  $Q_{flat} = 18 \mu\text{K}$ , the 61-m baseline image is expected to have a variance contribution  $(5.2 \mu\text{Jy beam}^{-1})^2$  from CMB anisotropy. Because (a) the two TFFs have only a small overlap and are largely sampling CMB power at different multipole ranges and (b) the 61-m baseline TFF has a greatly reduced sensitivity to CMB anisotropy, the confusion model that is derived from the 61-m baseline data is unlikely to significantly reduce the CMB anisotropy power expected in the residual 30.6-m baseline image.

We have simulated sky images by generating ‘flat’ spectrum CMB power in the  $(u, v)$ -plane: pixels of size  $\delta u, \delta v$  that are at distance  $\sqrt{u^2 + v^2}$  from the centre of the  $(u, v)$ -plane are given Gaussian random complex conjugate visibilities with variance

$$(\Delta T)^2 = (Q_{flat})^2 \left( \frac{6}{5\pi l^2} \right) \delta u \delta v. \quad (9)$$

The  $(u, v)$ -plane CMB anisotropy model is then filtered by the TFF corresponding to the 30.6-m baseline data and inverted to form simulated sky images. We have thereby obtained distributions of the sample variance from simulated images that have variance contribution from CMB anisotropy alone. It may be noted here that the radial distribution of power in the  $(u, v)$ -plane in the case of our ‘flat’ model CMB anisotropy differs from that for thermal noise and, therefore, the two contributions differ in the number of degrees of freedom in their contributions to image variance.

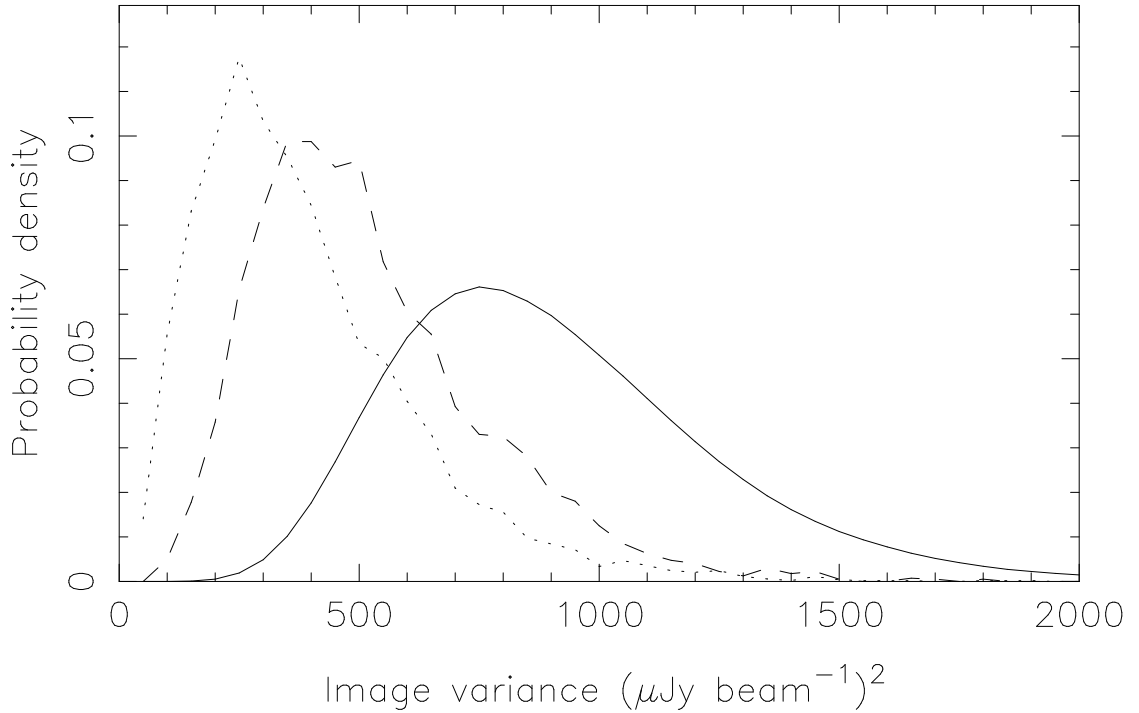


**Figure 7.** Likelihood functions. The dashed line corresponds to the null hypothesis  $\mathbb{H}_1$ , the continuous curve corresponds to the hypothesis  $\mathbb{H}_2$  that  $Q_{flat} = 22.4 \mu\text{K}$ . The dotted line corresponds to the distribution function assuming that ‘flat’ spectrum CMB anisotropy with  $Q_{flat} = 22.4 \mu\text{K}$  is the only contributor to the image variance.

## 5 LIMITS ON CMB FLAT-BAND POWER

We use the likelihood-ratio test to derive limits on possible CMB flat-band power in the data. We assume that the residual image has contributions only from the telescope thermal noise and possibly CMB anisotropy. The observed variance in the residual image shown in Fig. 4 is

$$\sigma_{obs}^2 = (21.2 \mu\text{Jy beam}^{-1})^2. \quad (10)$$

We adopt the null hypothesis  $\mathbb{H}_1$  that the variance contribution from CMB anisotropy is zero.

$$\mathbb{H}_1 : \sigma_{CMB}^2 = 0. \quad (11)$$

Simulations of sky images that have only thermal noise with an expected variance  $(22.8 \mu\text{Jy beam}^{-1})^2$  then yields the probability distribution for the sample variance. We show this distribution as the dashed line in Fig. 7 and represents the likelihood function  $\mathbb{P}(\sigma_{obs}^2 | 0)$  which is the probability of obtaining any observed variance conditional on  $\mathbb{H}_1$ .

We next hypothesize that the sky has flat-band CMB anisotropy quantified by the normalization  $Q_{flat}$ , *i.e.*,

$$\mathbb{H}_2 : \sigma_{CMB}^2 \text{ corresponding to } Q_{flat}. \quad (12)$$

We simulate sky images with purely CMB anisotropy to obtain the distribution function for its variance contribution; we show this distribution in Fig. 7 as a dotted line for the specific choice  $Q_{flat} = 22.4 \mu\text{K}$ . The distribution function for the observed image variance, with contributions from

thermal noise and CMB anisotropy, will be a convolution of the two individual probability distributions. This distribution, shown as a continuous curve in Fig. 7, represents the likelihood function  $\mathbb{P}(\sigma_{obs}^2 | Q_{flat})$  which is the probability of obtaining any observed variance conditional on  $\mathbb{H}_2$ .

The size  $\alpha$  of the test is the probability of rejecting  $\mathbb{H}_2$  when it is true (a type I error). For the choice  $Q_{flat} = 22.4 \mu\text{K}$ ,  $\alpha = 0.05$  and, therefore,  $Q_{flat} = 22.4 \mu\text{K}$  is a 95 per cent confidence upper limit.

The power  $\beta$  of the test is defined as:  $\beta = 1 -$  probability of accepting  $\mathbb{H}_2$  when  $\mathbb{H}_1$  is true (a type II error). For our choice of  $Q_{flat} = 22.4 \mu\text{K}$ , the power  $\beta = 0.47$ . In order to increase the power of the test to a value  $\beta = 0.5$ , we may increase the decision variance to  $\sigma_{obs}^2 = (21.8 \mu\text{Jy beam}^{-1})^2$  and change the hypothesis  $\mathbb{H}_2$  to correspond to a choice  $Q_{flat} = 23.6 \mu\text{K}$ . For this choice of parameters, the test will reject  $\mathbb{H}_2$  with size  $\alpha = 0.05$  (95 per cent confidence) and the test will simultaneously have a power  $\beta = 0.5$ .

To summarize, the ATCA observations of the field place an upper limit of  $Q_{flat} < 23.6 \mu\text{K}$  with 95 per cent confidence in an  $l$ -space filter that peaks at  $l = 4700$ . The filter has half-maximum values at  $l = 3350$  and  $6050$ .

## 6 LIMITS ON CMB ANISOTROPY WITH A GAUSSIAN-FORM AUTOCORRELATION FUNCTION

The CMB anisotropy is sometimes assumed to have a



**Table 1.** ATCA limits on GACF anisotropy models.

Coherence scale	Size of the test	Power of the test	CMB temperature rms	$\Delta T/T$
$\xi_c$	$\alpha$	$\beta$	$C_o^{\frac{1}{2}}$	$C_o^{\frac{1}{2}}/T_o$
0'5	0.05	0.44	58 $\mu$ K	$2.1 \times 10^{-5}$
0'5	0.05	0.50	63 $\mu$ K	$2.3 \times 10^{-5}$
1'0	0.05	0.44	42 $\mu$ K	$1.5 \times 10^{-5}$
1'0	0.05	0.50	45 $\mu$ K	$1.6 \times 10^{-5}$
2'0	0.05	0.44	63 $\mu$ K	$2.3 \times 10^{-5}$
2'0	0.05	0.50	68 $\mu$ K	$2.5 \times 10^{-5}$

$$T_o = 2.73 \text{ K}$$

Gaussian autocorrelation function (GACF). The sky temperature is modelled to have a Gaussian distribution with zero mean and the autocorrelation of the sky temperature is taken to be of the form

$$C(\xi) = C_o e^{-\left(\frac{\xi^2}{2\xi_c^2}\right)}. \quad (13)$$

Parameter  $C_o = \langle T^2(\theta, \phi) \rangle$  represents the variance of the sky temperature and parameter  $\xi_c = (-C'(0)/C''(0))^{\frac{1}{2}}$  represents the coherence scale ( $C''(\xi)$  denotes the second derivative of the autocorrelation function). Assuming that the coherence scale is a small angle, the power spectrum of the CMB temperature anisotropy may be approximately represented as  $l$ -space coefficients

$$C_l = 2\pi C_o \xi_c^2 e^{-\left(\frac{l^2 \xi_c^2}{2}\right)}. \quad (14)$$

This model may be expected to contribute an image variance

$$(\Delta S)^2 = \frac{1}{2} C_o \xi_c^2 \sum_l (2l+1) e^{-\left(\frac{l^2 \xi_c^2}{2}\right)} F_l \quad (15)$$

to the ATCA residual sky image. In this expression,  $\xi_c$  is the coherence scale in radians and  $F_l$  is the ATCA TFF corresponding to the variance estimate in the residual image of the observed field.

Assuming that the sky temperature variance  $C_o$  is an invariant, the expected image variance  $(\Delta S)^2$  is a maximum for an anisotropy model with  $\xi_c = 1$  arcmin. We have simulated sky images with the CMB anisotropy modelled to have a GACF and derived the distribution function for the image variance contribution. Limits to the model parameter  $C_o$  may be derived for specific choices of the coherence scale  $\xi_c$  using the likelihood ratio test described in the previous section.

Adopting a value  $\xi_c = 1$  arcmin, we find that the observed image variance of  $\sigma_{obs}^2 = (21.2 \mu\text{Jy beam}^{-1})^2$  implies a 95 per cent confidence upper limit of 42  $\mu$ K on  $C_o^{\frac{1}{2}}$ . This result corresponds to a test with size  $\alpha = 0.05$  and power  $\beta = 0.44$ . Requiring that the test have a power  $\beta$  of at least 0.5 relaxes the 95 per cent confidence upper limit to a value  $C_o^{\frac{1}{2}} = 45 \mu\text{K}$ . We have tabulated these limits along with those for models with coherence scales of 0.5 and 2 arcmin in Table 1.

## 7 A COMPARISON WITH OTHER MEASUREMENTS OF CMB ANISOTROPY

The best upper bounds reported to date in observations with the Owens Valley radio observatory (OVRO) is that the fractional fluctuations in the CMB sky is limited to  $\Delta T/T < 1.7 \times 10^{-5}$  at a resolution of 2 arcmin;  $C_o^{\frac{1}{2}}/T_o < 1.9 \times 10^{-5}$  in the case of fluctuations with a GACF and a coherence scale of 2'6 (OVRO NCP experiment: Readhead et al. 1989). Sensitive imaging observations with the Very Large Array (VLA) at 8.4 GHz have been used to place a limit of  $2.0 \times 10^{-5}$  on the fractional temperature fluctuations ( $\Delta T/T$ ) in the CMB at a resolution of 1 arcmin (VLA experiment: Partridge et al. 1997). Assuming that the CMB anisotropy has a GACF form, an upper limit of  $\Delta T/T \leq 2.1 \times 10^{-5}$  has been set for a coherence scale of 1'1 based on observations at 142 GHz using a 6-element bolometer array (SuZIE experiment: Church et al. 1997). The SuZIE observations have also been used to derive a  $2\sigma$  upper limit of  $Q_{flat} < 26 \mu\text{K}$  at an effective  $l \sim 2340$  (Ganga et al. 1997). Among these three observations, the first two have sensitivities per resolution element that are comparable to our ATCA observations. The SuZIE observations have covered a larger sky region. The ATCA observations presented in this work limit  $Q_{flat}$  to 23.6  $\mu\text{K}$  at  $l_{eff} = 4700$  and limit  $C_o^{\frac{1}{2}}/T_o$  to  $1.6 \times 10^{-5}$  for GACF form CMB anisotropy with  $\xi_c = 1$  arcmin. These different experiments attempting to measure the CMB anisotropy on arcmin scales have comparable upper limits on random phase CMB anisotropy at multipoles  $l > 1000$ .

## ACKNOWLEDGMENTS

The Australia Telescope is funded by the Commonwealth of Australia for operation as a National Facility managed by CSIRO. RS thanks Rajaram Nityananda for his interest and helpful suggestions.

## REFERENCES

- Aghanim N., Desert F. X., Puget J. L., Gispert R., 1996, *A&A*, 311, 1
- Bennett C. L. et al., 1996, *ApJ*, 464, L1
- Bond J. R., Myers S. T., 1996, *ApJS*, 103, 63
- Church S. E., Ganga K. M., Ade P. A. R., Holzapfel W. L., Mouskopf P. D., Wilbanks T. M., Lange A. E., 1997, *astro-ph* 9702196
- Ganga K., Ratra B., Church S. E., Sugiyama N., Ade P. A. R., Holzapfel W. L., Lange A. E., Mouskopf P. D., 1997, *astro-ph*

- 9702186  
 Gough R., 1994, Australia Telescope Technical Document AT/39.2/063  
 Hattori M. et al., 1997, Nature, 388, 146  
 Hu W., Scott D., Silk J., 1994, Phys. Rev. D, 49, 2  
 Hu W., Sugiyama N., 1994, ApJ, 436, 456  
 Hu W., Bunn E. F., Sugiyama N., 1995, ApJ, 447, L59  
 James G. L., 1985, IREECON'85 International Digest, p.713  
 James G. L., 1987, Proc. IEEE, 134, 217  
 Jones M. E. et al., 1997, ApJ, 479, L1  
 Lineweaver C. H., Barbosa D., 1997, astro-ph 9706077  
 Partridge R. B., Richards E. A., Fomalont E. B., Kellermann K. I., Windhorst R. A., 1997, ApJ, 483, 38  
 Persi F. M., Spergel D. N., Cen R., Ostriker J. P., 1995, ApJ, 442, 1  
 Readhead A. C. S., Lawrence C. R., Myers S. T., Sargent W. L. W., Hardebeck H. E., Moffet A. T., 1989, ApJ, 346, 566  
 Reynolds J., 1994, Australia Telescope Technical Document AT/39.3/040  
 Richards E. A., Fomalont E. B., Kellermann K. I., Partridge R. B., Windhorst R. A., 1997, NRAO preprint NRAO-96/238  
 Subrahmanyan R., Ekers R. D., Sinclair M., Silk J., 1993, MNRAS, 263, 416  
 The Australia Telescope, 1992, Special issue of: J. Electr. Electron. Eng. Aust., 12, June

## APPENDIX A: TELESCOPE FILTER FUNCTIONS (TFF)

In the case of CMB anisotropy experiments that are done using single-dish telescopes with a specified beam switching scheme, the telescope beam is usually described by a 2D function on the sky that is normalized to unit volume. The antenna temperature measured at any sky position is then the mean sky brightness temperature weighted by the beam pattern. The antenna temperatures obtained at a set of sky positions (that are defined by the beam switching scheme) are combined linearly to form an estimate of the CMB anisotropy. The ‘effective’ beam on the sky is the same linear combination of the 2D telescope beam patterns. The TFF corresponding to the estimate of the CMB anisotropy that is made with the ‘effective’ beam is the spherical harmonic decomposition of the ‘effective’ beam pattern.

In observations for CMB anisotropy made with Fourier synthesis telescopes, the sky temperature anisotropy is viewed by the array through the element primary beam pattern. The temperature anisotropy, attenuated by the primary beam pattern of the individual array element, is convolved by the synthesized beam pattern. The synthesized beam is normalized to peak unity and has zero volume. Unlike the case of the ‘effective’ beam in beam-switched, single-dish observations, the synthesized beam is not usually decomposable into a linear combination of identical (position shifted) beams that have finite volume. Therefore, the measurements (image pixel intensities) in Fourier synthesis images are integrals of the sky brightness temperature over the synthesized beam and cannot be converted to mean (or weighted mean) temperatures by normalising with any beam volume. The measurements will be in units of flux density (Jy) per beam rather than temperature.

For large multipole orders and small angles, the spherical harmonic decomposition may be approximated by a continuous Fourier transform and the  $C_l$ 's may be related to the

sky autocorrelation function  $C(\theta)$  by

$$C_l = 2\pi \int_0^\infty \theta d\theta C(\theta) J_0(l\theta). \quad (\text{A1})$$

Multipole order  $l/(2\pi)$  and angular distance  $\theta$  (in radians) are Fourier transform conjugates. If the ‘effective’ beam is a purely radial function  $b(\theta)$ , the TFF will be similarly given by

$$F_l = \left| 2\pi \int_0^\infty \theta d\theta b(\theta) J_0(l\theta) \right|^2. \quad (\text{A2})$$

If the ‘effective’ beam is not simply a radial function, one computes the 2D Fourier transform  $\mathbb{F}(l, \xi)$  of the 2D beam  $b(\theta, \phi)$  and circumferentially averages  $|\mathbb{F}(l, \xi)|^2$  to get the filter function  $F_l$ .

The TFF in Fourier synthesis images will vary across the image. At any image pixel location  $(\theta_o, \phi_o)$ , we first determine the ‘effective’ beam  $b(\theta, \phi)$  as the product of the primary beam centred at the antenna pointing centre and the synthesized beam centred at  $(\theta_o, \phi_o)$ . The two beams are separately normalized to have peak unity. The beam is Fourier transformed to give

$$\mathbb{F}(l, \xi) = \int \int b(\theta, \phi) e^{i(\theta l \cos \xi + \phi l \sin \xi)} d\theta d\phi. \quad (\text{A3})$$

The TFF is then derived as

$$F_l = \frac{1}{2\pi} \int_0^{2\pi} |\mathbb{F}(l, \xi)|^2 d\xi \left( \frac{2k}{\lambda^2} \right)^2. \quad (\text{A4})$$

$F_l$ , as defined in this form for Fourier-synthesis imaging, has units  $(\text{Jy beam}^{-1} \text{K}^{-1})^2$ .

If the image variance is computed as a linear combination of the squares of the pixel intensities (a weighted sum of squares), the TFF for the variance estimator may correspondingly be computed as the same linear combination of the  $F_l$ 's evaluated at the individual pixel locations.